Optimal Control of Vortex Shedding Using Low Order Models
Part I : Open-Loop Model Development

By W. R. GRAHAM[1] , J. PERAIRE[2] AND K. Y. TANG [2]

[1]Department of Engineering, University of Cambridge, Cambridge, CB2 1PZ, UK
[2]Department of Aeronautics and Astronautics, Massachusetts Institute of Technology, Cambridge, Ma 02139, U.S.A

(Received 5 December 1997)

An approach to developing active control strategies for separated flows is presented. The methodology proposed is applied to the incompressible unsteady wake flow behind a circular cylinder at a Reynold's number of 100. Control action is achieved via cylinder rotation. Low order models which are amenable to control and which incorporate the full non-linear dynamics are developed by applying the proper orthogonal decomposition technique to data provided by numerical simulation. This process involves extensions to the usual POD approach and the results are therefore assessed for two "open-loop" test cases. The predictions are found to be satisfactory for control purposes, assuming the model can be reset periodically. The use of these models for optimal control is discussed in a companion paper, Part II.

1. Introduction

With the advent of high speed micro-electronics, the concept of active control of the properties of a fluid flow has become accepted as a technical possibility, with many potential benefits and significant advantages over conventional passive control methods. To date, much of the work in this area has been directed towards the suppression of instabilities (Langhorne 1988, Bloxsidge et al 1988, Ffowcs Williams and Huang 1989, Ffowcs Williams and Graham 1990, Langhorne et al 1990, Gysling et al 1991, Pinsley et al 1991, Day 1993, Paduano et al 1993) and considerable progress has been made. However, a feature which appears to be common to many fluid flows is a rapid increase in the number of unstable modes beyond the threshold of stability. For example, Berger's (1967) attempts to suppress bluff-body vortex shedding by feedback control resulted in a very small increase in the critical Reynolds number (from 77-80 and from 80-83.5 in two different geometries), a result which Monkewitz et al (1991) have attributed to the appearance of a second (globally) unstable mode in the wake. Thus, in many cases of practical interest, the number of unstable modes may be too great to hope for their suppression, and instead the object of the control must be to ameliorate their effects (e.g. the unsteady lift on a vortex shedding body, or the buffet experienced by a surface in a separated flow).

This aspect of active flow control has to date received relatively little attention, and consequently the development of models which may be employed in control system design and implementation is at an early stage. The cases of interest here are likely to be too complex for the heuristic approach to model generation used in many instability suppression problems (e.g. Moore and Greitzer 1986, Ffowcs Williams and Huang 1989, Bloxsidge et al 1988) to be successful; nor, given the non-linear nature of such flows, is numerical linearization (e.g. Chicatelli and Richard 1993, Hall 1994, Hall et al 1994) likely to be a useful approach. Instead, we must seek low order models which incorporate the full, non-linear system dynamics. Such models may be obtained from experimental or computational data for the flow of interest and their feasibility depends, of course, on the dimensionality of the relevant flow features being relatively low.

In these cases, a well-established technique for extracting the dominant features (or degrees of freedom) from a sample data set is the Proper Orthogonal Decomposition (POD), which yields a set of orthogonal basis functions that are optimal in the sense of energy capture from the data set (Sirovich 1987, Berkooz et al 1993). These functions may be used as a basis for series expansions of the flow variables, and a Galerkin projection of the governing equations then yields a set of ordinary differential equations representing the system. This approach has been employed extensively in turbulence studies (see Berkooz et al 1993 for a comprehensive set of references), and also in examples of larger scale unsteadiness (e.g. Glezer et al 1989, Deane et al 1991, Rajaee et al 1994). However, with some exceptions (Deane et al 1991, Coller et al 1994), previous work has been largely descriptive, in that the low order model has generally been used to simulate the flow which gave rise to it. The technique will thus require development for our purposes, and in this paper (Part I) we discuss this process. In the companion paper (Part II), we describe the application of the resulting low order models to the control problem.

The test case we choose is the two-dimensional flow past a circular cylinder, with control action achieved via cylinder rotation. For Reynolds numbers above 50 (approximately) this example exhibits vortex shedding, and is generally regarded as a canonical unsteady, separated flow. We shall consider the case with Reynolds number 100 where, in the light of the above discussion, a single degree-of-freedom control action cannot be expected to suppress the shedding entirely, and we must instead concentrate on ameliorating its effects.

The flow data used to generate the low order model are provided by a numerical simulation, described in Sec. 2. The application of the POD to this data is then discussed in Sec. 3. In order to impose control action boundary conditions two extensions to the basis function derivation/Galerkin projection procedure are proposed in Sec. 4. The range of applicability of the resulting low order model is found to depend critically on the ability of the basis functions to describe sufficiently general solutions. The generation of suitable basis functions is addressed in Sec. 5, and the corresponding low order models are assessed by means of two "open-loop" test cases. The implications of the results here are then discussed in the light of the control to be implemented in Part II.

2. Numerical Simulation of the Cylinder Flow

We consider two-dimensional, incompressible channel flow of a fluid with density ρ past a circular cylinder of diameter D (see figure 1). The flow is governed by the continuity and Navier-Stokes equations which, in dimensionless form, are

$$\nabla \cdot \mathbf{u} = 0 \tag{2.1}$$

$$\frac{\partial \mathbf{u}}{\partial t} + (\mathbf{u} \cdot \nabla)\mathbf{u} = -\nabla p + \frac{1}{Re}\nabla^2 \mathbf{u} \tag{2.2}$$

where the velocity $\mathbf{u} = (u, v)$ has been non-dimensionalized on the inflow velocity U; the

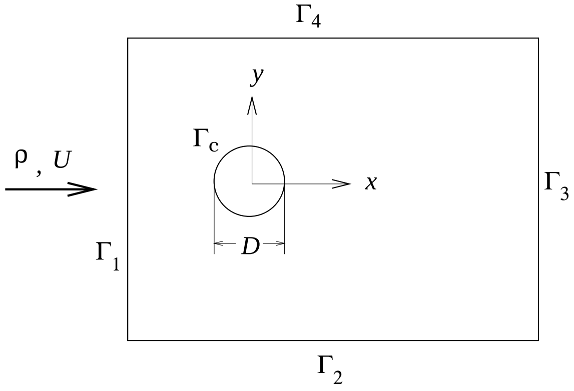

FIGURE 1. Simulation domain for circular cylinder flow problem

pressure p on ρU^2, time on D/U and spatial variables on D. The Reynolds number Re is defined as usual, $Re = \rho U D/\mu$, where μ is the fluid's dynamic viscosity.

The problem specification is completed by the boundary conditions

$$(u, v) = (1, 0) \qquad on \qquad \Gamma_1 \tag{2.3}$$

$$\frac{\partial u}{\partial y} = 0, \quad v = 0 \qquad on \qquad \Gamma_2, \Gamma_4 \tag{2.4}$$

$$p = 0, \qquad on \qquad \Gamma_3 \tag{2.5}$$

$$(u, v) = (-\gamma y,\ \gamma x) \qquad on \qquad \Gamma_c \tag{2.6}$$

where γ is the angular velocity of the cylinder. Equation (2.4) represents a zero shear stress condition at the channel side-walls, and equation (2.5) is found to be an acceptable approximation for conditions at the outflow, provided this boundary is placed at a sufficient distance downstream of the cylinder (see section 2.3).

2.1. *Discretization of the Equations*

Equations (2.1) and (2.2) are discretized in time via a three step projection method (Chorin 1969, Donea et al 1982) and in space using a Galerkin finite element approximation (Zienkiewicz et al 1990). The details of this process are described below, and results from numerical simulations of the discretized equation set are presented in section 2.2. Tang (1996) also discusses these subjects, in greater depth than space permits here.

2.1.1. *Time discretization*

The Navier-Stokes equations, (2.2), are discretized in time using forward Euler time-stepping via an intermediate velocity $\mathbf{u}^*$;

$$\frac{\mathbf{u}^* - \mathbf{u}^n}{\Delta t} = -(\mathbf{u}^n \cdot \nabla)\mathbf{u}^n + \frac{1}{Re}\nabla^2 \mathbf{u}^n \tag{2.7}$$

$$\frac{\mathbf{u}^{n+1} - \mathbf{u}^*}{\Delta t} = -\nabla p^n \tag{2.8}$$

where $\mathbf{u}^n$ denotes $\mathbf{u}(\mathbf{x}, t^n)$ and $t^{n+1} = t^n + \Delta t$. Before the latter step can be completed the pressure field at time level n must be found, and this is achieved by enforcing the continuity requirement, (2.1), on $\mathbf{u}^{n+1}$, giving

$$\nabla^2 p^n = \frac{\nabla \cdot \mathbf{u}^*}{\Delta t} \tag{2.9}$$

The numerical process thus consists of solving first equation (2.7), then (2.9) and finally (2.8). As $\mathbf{u}^*$ has no clear physical meaning, no boundary conditions are explicitly applied in the first step. By contrast, the boundary value problem represented by the second step, (2.9), requires conditions on p to be specified on all the boundary surfaces. With the exception of equation (2.5) for Γ_3, these can be derived from equation (2.8), which yields

$$\frac{\partial p}{\partial n} = \frac{(\mathbf{u}^* - \mathbf{u}^{n+1})}{\Delta t} \cdot \mathbf{n} \tag{2.10}$$

where $\mathbf{n}$ is the outward unit normal at the boundary surface. Once $\mathbf{u}^*$ is known, the velocity conditions given in equations (2.3), (2.4) and (2.6) thus specify $\partial p/\partial n$ on $\Gamma_1, \Gamma_2, \Gamma_4$ and Γ_c and equation (2.9) may then be solved for p^n. The final step, equation (2.8), now yields $\mathbf{u}^{n+1}$, and is carried out subject to the Dirichlet conditions on $\mathbf{u}$ specified in equations (2.3), (2.4) and (2.6).

In the absence of upwind spatial differencing, or added artificial viscosity, the formulation described here would suffer from the well-known numerical instability problems associated with the discretization of the convective term. Such difficulties may be avoided by replacing equation (2.7) by

$$\frac{\mathbf{u}^* - \mathbf{u}^n}{\Delta t} = -(\mathbf{u}^n \cdot \nabla)\mathbf{u}^n + \frac{1}{Re}\nabla^2 \mathbf{u}^n + \frac{\Delta t}{2}\nabla \cdot [(\mathbf{u}^n \otimes \mathbf{u}^n) \cdot \nabla \mathbf{u}^n] \tag{2.11}$$

where $\otimes$ denotes a dyadic product. The additional term plays the role of an added artificial viscosity which is only active in the streamline direction (Christie et al 1976, Hughes and Brooks 1979, Donea 1984) and despite having only a higher order effect, due to the presence of Δt, it is found to be sufficient to stabilize the numerical solution.

2.1.2. *Spatial discretization*

Equations (2.11), (2.9) and (2.8) are discretized in space using the Galerkin finite element method (see, for example, Zienkiewicz and Morgan 1982). Briefly, the two-dimensional domain Ω of figure 1 is discretized into a mesh of triangular elements, and linear shape functions $N_i(\mathbf{x})$ $[\mathbf{x} = (x, y)]$ are defined for each node i. Figure 2 shows the finite element mesh, consisting of 6650 triangles and 3401 vertices, used for the computations reported in this paper. The requirements that $N_i(\mathbf{x})$ be one at the node i, zero at all the other nodes, and be piecewise linear in x and y- coordinates over each triangular element are sufficient to specify it uniquely.

These shape functions may be used to approximate the problem variables $\mathbf{u}$ and p in a piecewise linear fashion

$$\mathbf{u} \approx \sum_i \mathbf{u}_i N_i(\mathbf{x}), \qquad p(\mathbf{x}) \approx \sum_i p_i N_i(\mathbf{x}) \tag{2.12}$$

where the summation extends over the total number of vertices, and $\mathbf{u}_i$ and p_i denote the values of the velocity and pressure at the mesh node i. A Galerkin projection procedure

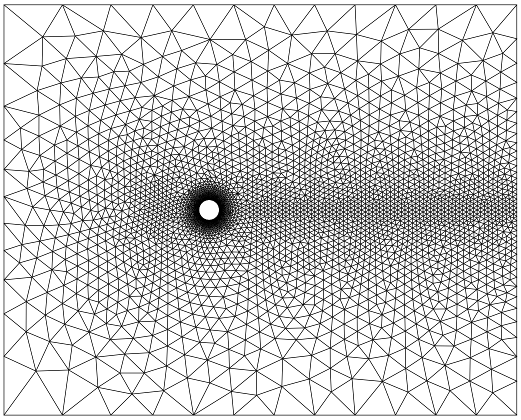

FIGURE 2. Finite Element Mesh (Diameter of Cylinder = 1 ; Upstream and Downstream Boundaries from Center of Cylinder = 10, 15 ; Width = 20)

enforcing orthogonality between the equation residuals and the $N_i(\mathbf{x})$ functions can now be used. Thus, from equation (2.11), we obtain for every node in the mesh an equation of the form

$$(N_i, \mathbf{u}^* - \mathbf{u}^n) = \Delta t\ (N_i, (\mathbf{u}^n \cdot \nabla)\mathbf{u}^n) - \frac{\Delta t}{Re}(\nabla N_i, \nabla \mathbf{u}^n) - \frac{\Delta t^2}{2}(\nabla N_i, (\mathbf{u}^n \otimes \mathbf{u}^n) \cdot \nabla \mathbf{u}^n) + \frac{\Delta t}{Re}[N_i \nabla \mathbf{u}^n] + \frac{\Delta t^2}{2}[N_i(\mathbf{u}^n \otimes \mathbf{u}^n) \cdot \nabla \mathbf{u}^n] \qquad (2.13)$$

where

$$(\mathbf{a}, \mathbf{b}) = \int_\Omega \mathbf{a} \cdot \mathbf{b}\ d\Omega; \quad (\alpha, \mathbf{a}) = \int_\Omega \alpha \mathbf{a}\ d\Omega; \quad [\mathbf{a}] = \int_{\Gamma_1 \cap \Gamma_2 \cap \Gamma_3 \cap \Gamma_4 \cap \Gamma_c} \mathbf{a} \cdot \mathbf{n}\ d\Gamma \qquad (2.14)$$

Note that integration by parts has been employed to reduce the order of the derivatives in the viscous and artificial viscosity terms. On expressing $\mathbf{u}^n$ and $\mathbf{u}^*$ in the approximate form of equation (2.12), the problem is then reduced to the algebraic equation set

$$\sum_j M_{ij}(\mathbf{u}_j^* - \mathbf{u}_j^n) = \mathbf{r}_i^I \qquad (2.15)$$

where $M_{ij} = (N_i, N_j)$ is the finite element consistent mass matrix and $\mathbf{r}_i^I$ is straightforwardly calculated in terms of the (known) $\mathbf{u}_i^n$ from equation (2.13). The value of $\nabla \mathbf{u}^n \cdot \mathbf{n}$ on the boundary is either determined from the boundary conditions (for Γ_2 and Γ_4), or approximated by its value inside the element whose edge is the boundary component under consideration. The details of this process are standard (see, for example, Zienkiewicz and Morgan 1982), and will not be discussed here.

The second step of the numerical method, equation (2.9), has the Galerkin form

$$(\nabla N_i, \nabla p^n) = -\frac{1}{\Delta t}(N_i, \nabla \cdot \mathbf{u}^*) + [N_i \nabla p^n] \qquad (2.16)$$

where integration by parts has again been used to reduce the order of the derivatives appearing. The above equation is formed for every node i in the mesh with the exception of those on Γ_3, where the pressure is determined from the boundary condition of equation (2.5). The derivative of the pressure in the direction normal to the boundary on the remaining boundaries is evaluated from equation (2.10). Inserting the approximations (2.12) for $\mathbf{u}^*$ and p^n then yields an equation of the form

$$\sum_j K_{ij} p_j^n = r_i^{II} \tag{2.17}$$

where $K_{ij} = (\nabla N_i, \nabla N_j)$.

Finally, the third step, equation (2.8), becomes

$$(N_i, \mathbf{u}^{n+1} - \mathbf{u}^*) = -\Delta t \ (N_i, \nabla p^n) \tag{2.18}$$

and the usual substitutions yield an equation set analogous to (2.15),

$$\sum_j M_{ij} (\mathbf{u}_j^{n+1} - \mathbf{u}_j^*) = \mathbf{r}_i^{III} \tag{2.19}$$

The Dirichlet boundary conditions on $\mathbf{u}$ specified in equations (2.3), (2.4) and (2.6) are imposed here, so the set of weighting functions excludes those associated with the corresponding boundary nodes.

The finite element spatial discretization thus yields three matrix equations whose solution represents our numerical approximation to the flow. Furthermore, due to the strongly local nature of the shape functions, the matrices in these equations are sparse, and amenable to solution by iterative methods. Here a preconditioned conjugate gradient algorithm with a diagonal preconditioning matrix (see for instance Golub and Van Loan 1981) is employed. In addition, for equation (2.17) an initial guess (based on its prior history) is made for the pressure, to speed the solution. With convergence defined by a reduction in the squared equation residual of eight orders of magnitude, averages of 7 iterations per velocity component in steps 1 and 3, and around 50 iterations in step 2, are required for the mesh shown in figure 2.

2.2. *Simulation Results*

The simulations are performed at a Reynolds number of 100, where vortex shedding is well-established as the stable long term flow and results are available from previous investigations (e.g. Simo and Armero 1994) for comparison. An example of a typical long term flow solution is given in figure 3, which shows instantaneous pressure contours. The vortex street behind the cylinder is clearly visible, and no spurious reflections from the downstream boundary appear, supporting our earlier assertion regarding the acceptability of equation (2.5) as a boundary condition here.

The (dimensionless) force on the cylinder is given by

$$\mathbf{F} = (F_x, F_y) = \int_{\Gamma_c} (p\mathbf{n} - \frac{1}{Re}\frac{\partial \mathbf{u}}{\partial n}) \ d\Gamma \tag{2.20}$$

an integral which is straightforward to estimate given the nodal values of p and $\mathbf{u}$. The lift and drag coefficients are given by $C_L = 2F_y$ and $C_D = 2F_x$. Time histories of these quantities after the long term behavior has been established are plotted in figure 4. The mean value of C_D is 1.34, and the unsteady C_L and C_D amplitudes are 0.33 and 0.01 respectively. These values are somewhat (ca. 10-13%) lower than those shown by Simo

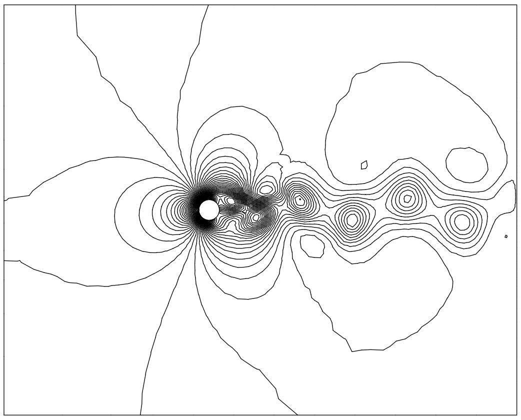

FIGURE 3. Pressure contours

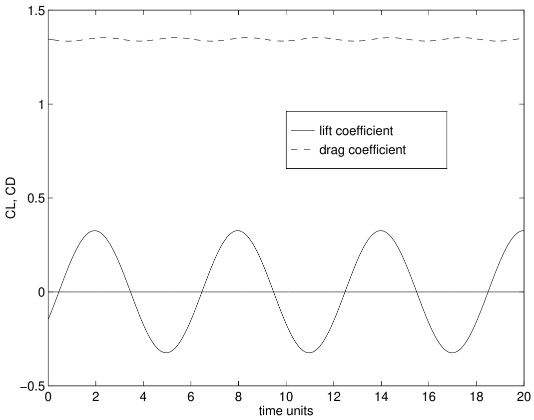

FIGURE 4. Lift and Drag Coefficient History

(1994); however an alternative, variational, formulation was found to yield very similar results, around 3% higher than the values quoted. Experimental data for the unsteady amplitudes are not readily available in the literature, but Duncan et al (1970) give a plot of mean C_D vs Re which yields $C_D \approx 1.4$ at $Re = 100$, in reasonable agreement with our predictions. Additionally, the dimensionless shedding period predicted here is 6.01, which yields a Strouhal number St ($= fD/U$, where f is the shedding frequency) of 0.168, in excellent agreement with Simo (1994) and the references quoted therein. Finally, results obtained by Tang (1996) at $Re = 200$ also compare well with previous numerical investigations.

3. Proper Orthogonal Decomposition of the Cylinder Flow

In recent years, the Proper Orthogonal Decomposition (POD) has become popular as a means of extracting dominant energy-containing structures from flow field data and, by using these structures as basis functions, generating low order dynamical models for the associated systems. As noted in the introduction, many of the studies in this area have been in the field which originally motivated the POD, turbulence, but the technique has also found application for a number of larger scale flows. Here we briefly describe the general POD approach (further details may be found in Sirovich 1987), before moving on to discuss its implementation, and its utility in the construction of a low order model for the flow past a stationary cylinder.

Given a flow field $\mathbf{u}(\mathbf{x},t)$, and a set of realizations or "snapshots" $\mathbf{u}(\mathbf{x},t^k)$, corresponding to K different instants in time, consider the following decomposition

$$\mathbf{u}(\mathbf{x},t) = \mathbf{u}_m(\mathbf{x}) + \mathbf{v}(\mathbf{x},t) \tag{3.1}$$

where $\mathbf{u}_m(\mathbf{x})$ is the flow mean value obtained as the arithmetic average of the snapshots. A two point spatial correlation matrix can be defined

$$\mathbf{K}(\mathbf{x},\mathbf{x}') = \frac{1}{K}\sum_{k=1}^{K} \mathbf{v}(\mathbf{x},t^k) \otimes \mathbf{v}(\mathbf{x}',t^k) \tag{3.2}$$

which accepts the following diagonal decomposition

$$\mathbf{K}(\mathbf{x},\mathbf{x}') = \sum_{k=1}^{K} \lambda_k \mathbf{\Psi}_k(\mathbf{x}) \otimes \mathbf{\Psi}_k(\mathbf{x}') \tag{3.3}$$

where the set of basis functions (or "modes") $\mathbf{\Psi}_k(\mathbf{x})$ are orthonormal (i.e. $(\mathbf{\Psi}_k,\mathbf{\Psi}_l) = \delta_{kl}$) and such that the eigenvalues are ordered ($\lambda_k \geq \lambda_{k+1}$), positive ($\lambda_k \geq 0$), and quantify the "energy" of the data set associated with the corresponding mode $\mathbf{\Psi}_k$,

$$\lambda_k = \frac{1}{K}\sum_{l=1}^{K} (\mathbf{\Psi}_k(\mathbf{x}),\mathbf{v}(\mathbf{x},t^l))^2 \tag{3.4}$$

It can be shown that the sum of all the eigenvalues represents the average unsteady energy in the data set. The set of functions $\mathbf{\Psi}_k(\mathbf{x})$ form a proper orthogonal decomposition (POD) and are optimal in the sense that (for a given $K' < K$) the approximate representation of the "snapshots"

$$\hat{\mathbf{v}}(\mathbf{x},t^l) = \sum_{k=1}^{K'} y_k^l \mathbf{\Psi}_k(\mathbf{x}), \qquad y_k^l = (\mathbf{\Psi}_k(\mathbf{x}),\mathbf{v}(\mathbf{x},t^l)) \tag{3.5}$$

maximizes the captured energy

$$\hat{E} = \frac{1}{K}\sum_{l=1}^{K} (\hat{\mathbf{v}}(\mathbf{x},t^l),\hat{\mathbf{v}}(\mathbf{x},t^l)) = \sum_{k=1}^{K'} \lambda_k \tag{3.6}$$

The first few $\mathbf{\Psi}_k(\mathbf{x})$ thus represent the main energy-containing structures in the data set, with their relative importance quantified by the λ_k.

3.1. *Derivation of POD basis functions*

As shown by Sirovich (1987), an efficient procedure for calculating the POD basis functions in situations where the number of degrees of freedom, or parameters, required to describe $\mathbf{u}(\mathbf{x},t^k)$ is larger than the number of snapshots K (i.e. when sampling highly resolved flows), consists of expressing the basis function $\mathbf{\Psi}_k$ as a linear combination of the snapshots

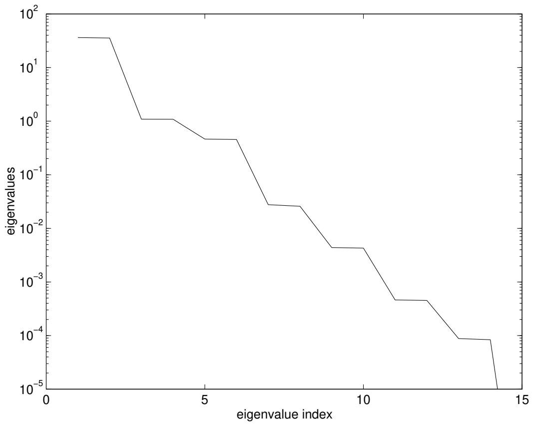

FIGURE 5. Eigenvalue spectrum (unforced vortex shedding)

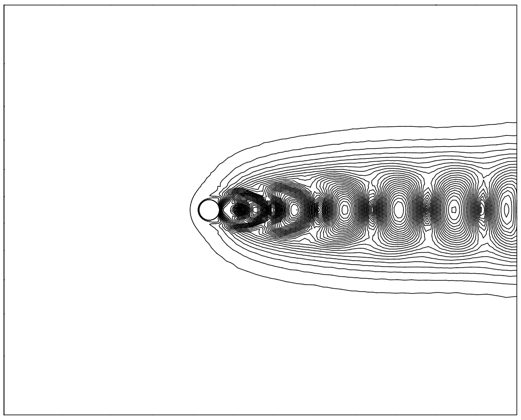

FIGURE 6. Velocity contours for the first mode

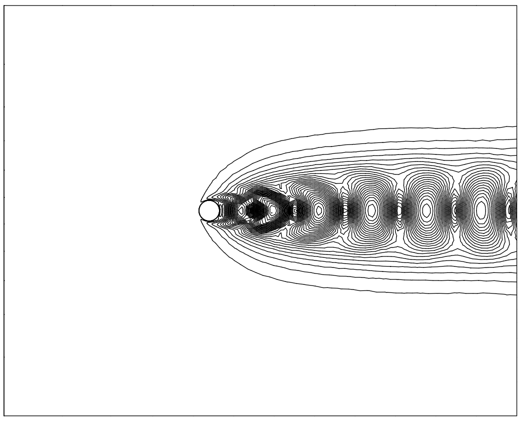

FIGURE 7. Velocity contours for the second mode

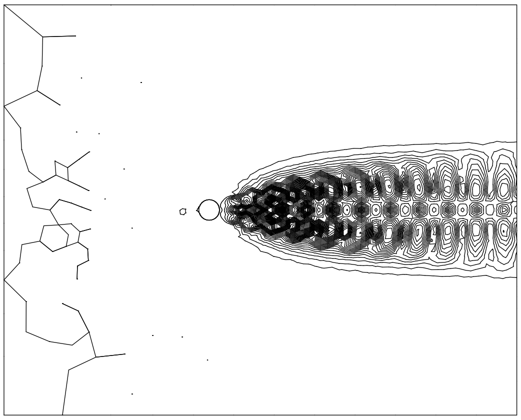

FIGURE 8. Velocity contours for the third mode

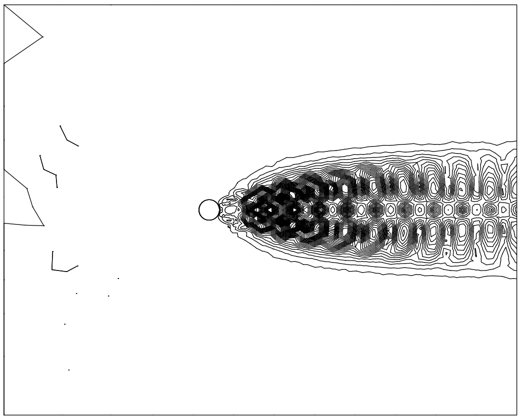

FIGURE 9. Velocity contours for the fourth mode

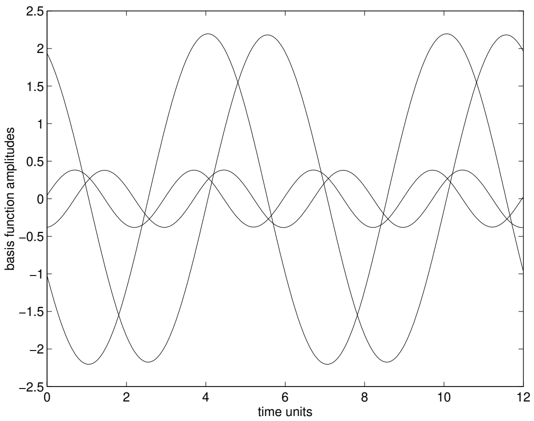

FIGURE 10. Mode amplitudes for the first four modes

$$\mathbf{\Psi}_k(\mathbf{x}) = \sum_{l=1}^{K} a_l \mathbf{v}(\mathbf{x}, t^l) \tag{3.7}$$

The constants a_l can then be determined by solving the following eigenvalue problem

$$\sum_{m=1}^{K} C_{lm} a_m = (K\lambda_k) a_l \tag{3.8}$$

where C_{lm} is the correlation matrix whose entries are $(\mathbf{v}(\mathbf{x}, t^l), \mathbf{v}(\mathbf{x}, t^m))$. These inner products are easily computed, with the aid of the finite element consistent mass matrix (equation 2.15), and the corresponding eigenvalues and eigenvectors are found from a singular value decomposition of the matrix.

Figure 5 shows the eigenvalue spectrum $(K\lambda_k)$ from the correlation matrix formed from a set of 15 snapshots of the cylinder flow, obtained at regular intervals over two vortex shedding periods. Clearly, most of the fluctuation energy is captured by the first two modes alone, and if six modes are taken the remaining eigenvalues account for less than 0.1% of the unsteadiness in the snapshots. The decomposition of the flow achieved here is thus highly efficient. These results are in agreement with those of Deane et al (1991), and the associated basis functions also correspond satisfactorily. Velocity contours for the first four are plotted in figures 6 to 9.

Note the pairing of similar patterns, shifted spatially, a result of the convective nature of the flow. The amplitudes of these basis functions present in the snapshots are plotted in figure 10, from which it is clear that the basis functions correspond very closely to the coefficients of a temporal Fourier series expansion of the periodic flow. This correspondence would be exact for a perfectly convective flow (Berkooz et al 1993); here it is remarkably close to being so, even for the higher basis functions/Fourier coefficients. An interesting corollary is that the mean flow (the zero'th Fourier coefficient) is very nearly orthogonal to the basis functions, and may (very nearly) be found as a mode if the correlation matrix is formed without first subtracting it from the snapshots.

3.2. *POD Low Order Model for the Flow Past a Stationary Cylinder*

As used above, the POD has a purely descriptive nature. However, the basis functions it produces may be used to generate a predictive model via a Galerkin projection of the Navier-Stokes equations. Often, the number of degrees of freedom required for this model to be accurate is small, and a significant decrease in complexity is achieved in comparison to the original system. To that end, consider the following expansion for the velocity field

$$\mathbf{u}(\mathbf{x}, t) = \mathbf{u}_m(\mathbf{x}) + \sum_{i=1}^{N} y_i(t) \mathbf{\Psi}_i(\mathbf{x}) \tag{3.9}$$

where $N(\leq K)$ is the size of the expansion. The Galerkin approximation to equation (2.2) is then

$$(\mathbf{\Psi}_i, \frac{\partial \mathbf{u}}{\partial t} + (\mathbf{u} \cdot \nabla)\mathbf{u}) + (\mathbf{\Psi}_i, \nabla p) = -\frac{1}{Re}(\nabla \mathbf{\Psi}_i, \nabla \mathbf{u}) + \frac{1}{Re}[\mathbf{\Psi}_i \nabla \mathbf{u}] \tag{3.10}$$

Since the basis functions $\mathbf{\Psi}_i$ are divergence-free by construction, (see (3.7)),

$$(\mathbf{\Psi}_i, \nabla p) = [p\mathbf{\Psi}_i] \tag{3.11}$$

which is equal to zero, since $\mathbf{\Psi}_i \cdot \mathbf{n} = 0$ on the surfaces $\Gamma_1, \Gamma_2, \Gamma_4$ and Γ_c, and $p = 0$ on Γ_3 (Sirovich 1987). Substitution of equation (3.9) into (3.10) then yields the following set of evolution equations for the mode amplitudes $y_i(t)$:

$$\frac{dy_i}{dt} = a_i + \sum_{j=1}^{N} b_{ij} y_j + \sum_{j=1}^{N} \sum_{k=1}^{N} c_{ijk} y_j y_k \tag{3.12}$$

where the coefficients are given by

$$a_i = -(\mathbf{\Psi}_i,\ (\mathbf{u}_m \cdot \nabla)\mathbf{u}_m) - \frac{1}{Re}(\nabla\mathbf{\Psi}_i, \nabla\mathbf{u}_m) + \frac{1}{Re}[\mathbf{\Psi}_i \nabla\mathbf{u}_m] \tag{3.13}$$

$$\begin{aligned} b_{ij} = -(\mathbf{\Psi}_i, (\mathbf{\Psi}_j \cdot \nabla)\mathbf{u}_m) - (\mathbf{\Psi}_i, (\mathbf{u}_m \cdot \nabla)\mathbf{\Psi}_j) - \\ \frac{1}{Re}(\nabla\mathbf{\Psi}_i, \nabla\mathbf{\Psi}_j) + \frac{1}{Re}[\mathbf{\Psi}_i \nabla\mathbf{\Psi}_j] \end{aligned} \tag{3.14}$$

$$c_{ijk} = -(\mathbf{\Psi}_i, (\mathbf{\Psi}_j \cdot \nabla)\mathbf{\Psi}_k) \tag{3.15}$$

After forming the coefficients from the first six basis functions, equation (3.12) is readily integrated from a given set of initial conditions (here a fourth order Runge-Kutta scheme is employed) yielding a set of predicted time histories for the mode amplitudes which may be compared with the projection of the numerical simulation onto these functions. As shown in figure 11, the integrated time histories for the first two modes match the observed results extremely well, while the amplitudes of the higher modes are only slightly less accurately predicted. This again agrees with the results of Deane et al (1991) and, as they did, we conclude that a 6 mode model provides an entirely satisfactory description of the long term dynamics for this case.

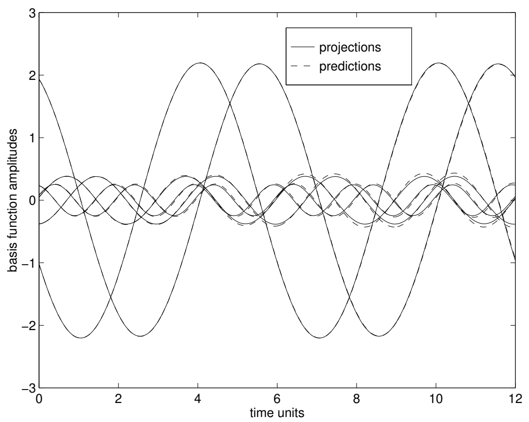

FIGURE 11. Comparison between predicted and projected mode amplitudes

4. Incorporation of Control Surface Motion into the Low Order Model

We now consider the situation in which the cylinder is set into an oscillatory rotation at frequencies close to the natural shedding frequency. In this case, the flow "locks on" (synchronizes with the cylinder rotation) and the vortex shedding becomes stronger. On performing the POD as described previously, we find that the eigenvalue spectrum is still concentrated around the first few modes (figure 12), and that the modes have similar structure to those derived for the stationary cylinder. However, since the cylinder is now rotating, the velocity expansion in equation (3.9) is no longer a valid candidate for $\mathbf{u}$ in the Galerkin projection, as it does not automatically satisfy the boundary conditions for arbitrary values of y_i.

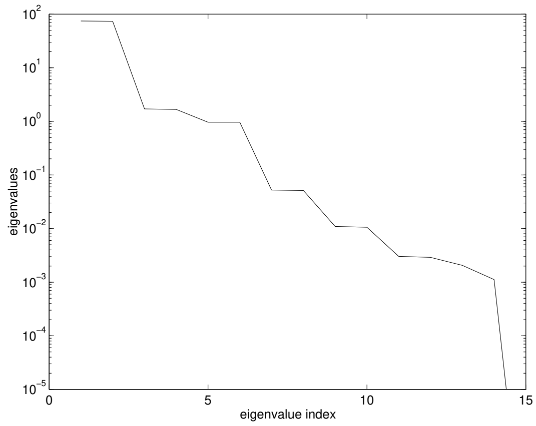

FIGURE 12. Eigenvalue spectrum (locked-on flow)

In this section we present two approaches which address this situation. The first, which we call the "control function method", is motivated by the desirability of having homogeneous boundary conditions on the basis functions used in the Galerkin projection, and involves the removal of the inhomogeneous boundary condition by including a suitably chosen function (the "control function") in the expansion for the velocity field. The second, the "penalty method" retains the POD basis functions in their original form, and imposes the inhomogeneous boundary condition in a weak sense when performing the Galerkin projection. Both formulations are formally valid, but yield qualitatively different low order models, and it is thus of interest to compare their performance.

4.1. *The control function method*

In this approach we remove the inhomogeneous boundary condition on Γ_c by subtracting a suitable "control function" from each snapshot before generating the POD basis functions. To retain the divergence-free property of the basis functions, our control function must also be divergence-free; we additionally require that it satisfies the appropriate (homogeneous) boundary conditions on Γ_1, Γ_2 and Γ_4. Beyond this, the function is arbitrary. A convenient way to generate it is to take the flow solution generated by the simulation for the desired motion of the boundary. Here, this is simply a steady cylinder rotation with angular velocity $\gamma = 1$. Denoting this solution by $\mathbf{u}_c(\mathbf{x})$, the modified snapshot set is now

$$\mathbf{u}(\mathbf{x}, t^k) - \gamma(t^k)\mathbf{u}_c(\mathbf{x}) \tag{4.1}$$

and the mean flow and basis functions are obtained from this modified set in the usual way. The $\mathbf{\Psi}_i$ thus generated have zero velocity on the cylinder surface, and the velocity expansion

$$\mathbf{u}(\mathbf{x},t) = \mathbf{u}_m(\mathbf{x}) + \gamma(t)\mathbf{u}_c(\mathbf{x}) + \sum_{i=1}^{N} y_i(t)\mathbf{\Psi}_i(\mathbf{x}) \tag{4.2}$$

therefore automatically satisfies the boundary conditions of the problem. On substituting this expansion into the Galerkin projection, equation (3.10), we obtain the following system of equations:

$$\frac{dy_i}{dt} = a_i + \sum_{j=1}^{N} b_{ij}y_j + \sum_{j=1}^{N}\sum_{k=1}^{N} c_{ijk}y_jy_k + d_i\frac{d\gamma}{dt} + (e_i + \sum_{j=1}^{N} f_{ij}y_j)\gamma + g_i\gamma^2 \tag{4.3}$$

where (in terms of our altered $\mathbf{\Psi}_i$'s) a_i, b_{ij} and c_{ijk} are given by equations (3.13) to (3.15), and

$$d_i = -(\mathbf{\Psi}_i, \mathbf{u}_c) \tag{4.4}$$

$$e_i = -(\mathbf{\Psi}_i, (\mathbf{u}_m\cdot\nabla)\mathbf{u}_c) - (\mathbf{\Psi}_i,\ (\mathbf{u}_c\cdot\nabla)\mathbf{u}_m) - \frac{1}{Re}(\nabla\mathbf{\Psi}_i, \nabla\mathbf{u}_c) + \frac{1}{Re}[\mathbf{\Psi}_i\nabla\mathbf{u}_c] \tag{4.5}$$

$$f_{ij} = -(\mathbf{\Psi}_i, (\mathbf{\Psi}_j\cdot\nabla)\mathbf{u}_c) - (\mathbf{\Psi}_i, (\mathbf{u}_c\cdot\nabla)\mathbf{\Psi}_j) \tag{4.6}$$

$$g_i = -(\mathbf{\Psi}_i, (\mathbf{u}_c\cdot\nabla)\mathbf{u}_c) \tag{4.7}$$

Given initial conditions on the coefficients y_i, and a prescribed time history for γ, these equations may be integrated forwards to yield predicted values of y_i, and hence predicted flow fields.

4.2. *The penalty method*

In this approach the essential boundary condition is enforced in an integral, "weak" fashion. The velocity on the cylinder surface is written as

$$\mathbf{u} = \gamma R\mathbf{e}_\theta - \epsilon\frac{\partial\mathbf{u}}{\partial n} \tag{4.8}$$

where $R(=1/2)$ is the cylinder radius, $\mathbf{e}_\theta$ the unit tangent vector and ϵ a small parameter. We can then replace our essential boundary condition with the alternative, natural boundary condition

$$\frac{\partial\mathbf{u}}{\partial n} = -\frac{\mathbf{u} - \gamma R\mathbf{e}_\theta}{\epsilon} \tag{4.9}$$

which may be imposed in a weak sense via surface integral terms in the Galerkin projection (Zienkiewicz and Morgan 1982). As $\epsilon \to 0$, $\mathbf{u}$ on the cylinder boundary will converge to the original boundary condition. Essentially, this approach may be thought of as setting $\mathbf{u}$ equal to the velocity a distance ϵ into the fluid, and reducing that distance until a satisfactory solution is obtained.

In this case, on performing the Galerkin projection, we obtain

$$\frac{dy_i}{dt} = a_i^p + \sum_{j=1}^{N} b_{ij}^p y_j + \sum_{j=1}^{N}\sum_{k=1}^{N} c_{ijk} y_j y_k + d_i^p \gamma \tag{4.10}$$

where

$$a_i^p = -(\mathbf{\Psi}_i,\ (\mathbf{u}_m\cdot\nabla)\mathbf{u}_m) - \frac{1}{Re}(\nabla\mathbf{\Psi}_i, \nabla\mathbf{u}_m) + \frac{1}{Re}[\mathbf{\Psi}_i\nabla\mathbf{u}_m] - \frac{1}{Re}\int_{\Gamma_c}\mathbf{\Psi}_i\cdot(\frac{\mathbf{u}_m}{\epsilon} + \frac{\partial\mathbf{u}_m}{\partial n})\ d\Gamma \tag{4.11}$$

$$b_{ij}^p = -(\mathbf{\Psi}_i,\ (\mathbf{\Psi}_j\cdot\nabla)\mathbf{u}_m) - (\mathbf{\Psi}_i,\ (\mathbf{u}_m\cdot\nabla)\mathbf{\Psi}_j) - \frac{1}{Re}(\nabla\mathbf{\Psi}_i, \nabla\mathbf{\Psi}_j) + \frac{1}{Re}[\mathbf{\Psi}_i\nabla\mathbf{\Psi}_j] - \frac{1}{Re}\int_{\Gamma_c}\mathbf{\Psi}_i\cdot(\frac{\mathbf{\Psi}_j}{\epsilon} + \frac{\partial\mathbf{\Psi}_j}{\partial n})d\Gamma \tag{4.12}$$

the definition of c_{ijk} is unchanged from equation (3.11), and

$$d_i^p = \frac{1}{\epsilon Re}\int_{\Gamma_c}\mathbf{\Psi}_i\cdot(R\mathbf{e}_\theta)d\Gamma \tag{4.13}$$

Note that, even though our $\mathbf{\Psi}_i$ are non-zero on the cylinder surface, $\mathbf{\Psi}\cdot\mathbf{n} = 0$ still; hence the continued absence of the pressure term. As with the control function formulation, equation (4.10) may be integrated forwards in time, subject to a set of initial conditions and specified $\gamma(t)$, to yield predictions for the mode amplitudes.

4.3. *Discussion*

Equations (4.3) and (4.10) are of markedly different form, and some discussion of the two approaches leading to them is warranted. The control function method has the advantages of explicitly enforcing the desired boundary conditions, and of ensuring that the Galerkin projection of the ∇p term in equation (3.3) disappears even in the more general case where the boundary moves normal to itself. On the other hand, it leads to a cumbersome formulation in comparison to the penalty method, and this complexity would increase with less restricted forms of control surface motion, where more control functions would be required to parameterize the boundary condition.

By contrast, the penalty method requires no parameterization of the surface motion, but would lead to a formulation involving pressure for boundary conditions with velocity components normal to the surface (since our $\mathbf{\Psi}_i$ would, in general, be non-zero there). This difficulty is not insurmountable, as it would be quite possible to calculate the pressure in parallel with the velocity via an extended low order model. In fact, this requirement reflects the more physical nature of the penalty method formulation, which associates the influence of tangential boundary motion with the viscous term, and the influence of normal boundary motion with the pressure, as one would expect.

The only other drawback of the penalty method is the introduction of the parameter ϵ, for which appropriate values cannot be determined a priori. However, values giving converged answers are relatively easy to find by numerical experimentation.

4.4. *Low Order Models for the Locked-On Flow*

Having developed methods to cope with inhomogeneous boundary conditions at the cylinder surface, we can reconsider the low order model for locked-on flow. Here the cylinder is driven at an angular velocity $\gamma = 2sin\frac{2\pi t}{6}$. This frequency corresponds to that of natural vortex shedding. Given a set of snapshots from this flow, the standard POD yields the $\mathbf{\Psi}_i$ for the penalty method, while the modified approach described above gives $\mathbf{\Psi}_i$ suitable for the control function method. The results of six mode integrations of the two low order formulations, and the projections of the simulation onto the basis functions, are plotted in figures 13 and 14. (A value of 0.001 for ϵ was found to yield a satisfactory converged solution for the penalty method.) The predictions of both methods show accuracy comparable to the stationary cylinder results (figure 11).

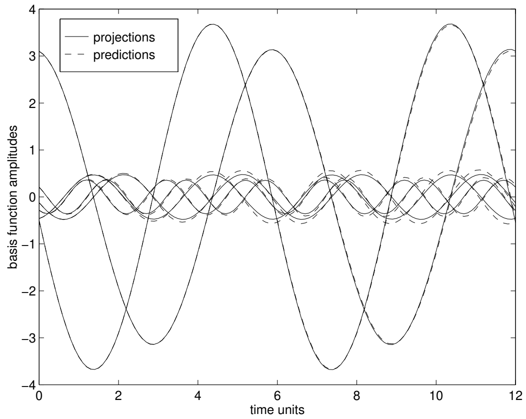

FIGURE 13. Locked-on flow (control function method)

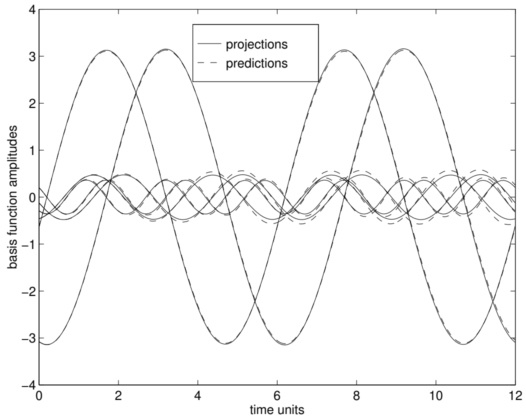

FIGURE 14. Locked-on flow (penalty method)

Next, we investigate the ability of these models to describe the effect of a change in the cylinder motion; namely a halt at the instant when the angular velocity is zero. The results for the first two modes are shown in figures 15 and 16. In each case, the predictions of the models are seriously in error. For the control function method large errors in amplitude and phase develop, whereas for the penalty method the predictions are still worse—in this case the model completely misses the system dynamics. The source of the problem lies in the highly-tuned basis functions, which essentially tie the predicted flow downstream of the cylinder to that at the cylinder. In particular, for the penalty method, the strong coupling between the rotation and the first two mode amplitudes quickly drives their levels to zero. While this tuning feature is acceptable in the steady-state conditions previously considered, it is incapable of following a change of phase in the vortex shedding, or other variation at the cylinder, while simultaneously modeling the downstream convection of existing flow structures. To achieve a broader set of basis functions which possess this capability, it is necessary to exercise more care in the snapshot generation process, and this issue is discussed in the following section.

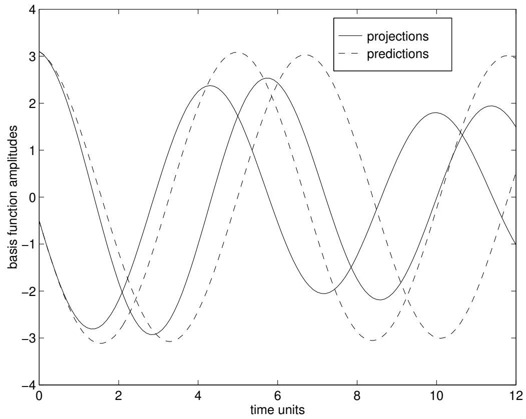

FIGURE 15. Sudden halt of a locked-on flow (control function method)

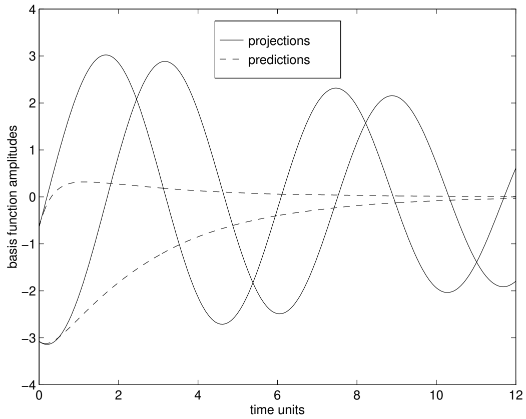

FIGURE 16. Sudden halt of a locked-on flow (penalty method)

5. Generalized Basis Functions

In the previous section we showed that basis functions derived from the steady-state locked-on flow were incapable of successfully capturing the flow dynamics due to a change in the cylinder rotation pattern (in this case from sinusoidal to stationary). Since this problem is associated with the unphysical coupling of conditions at the cylinder with conditions downstream, we seek a method of generating snapshots which de-couples these

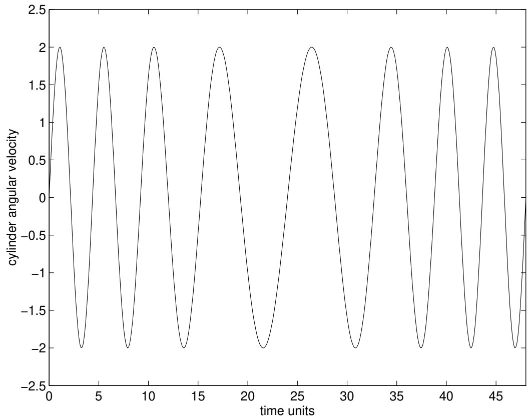

FIGURE 17. Time history of the chirp excitation

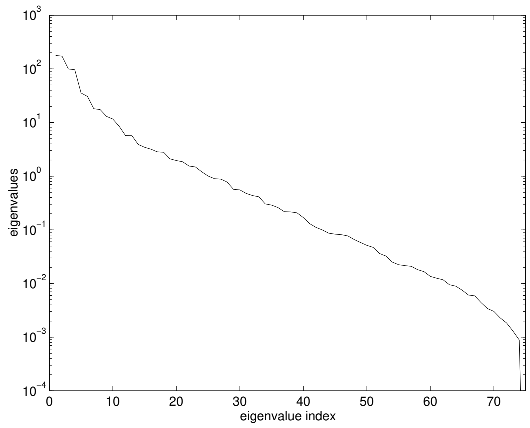

FIGURE 18. Eigenvalue spectrum (chirp excitation, locked-on initial condition)

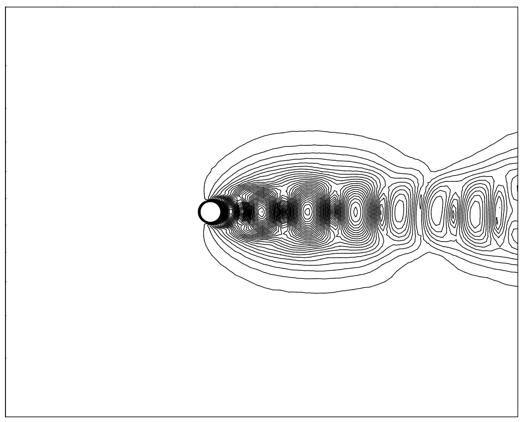

FIGURE 19. Mode velocity contours (example 1)

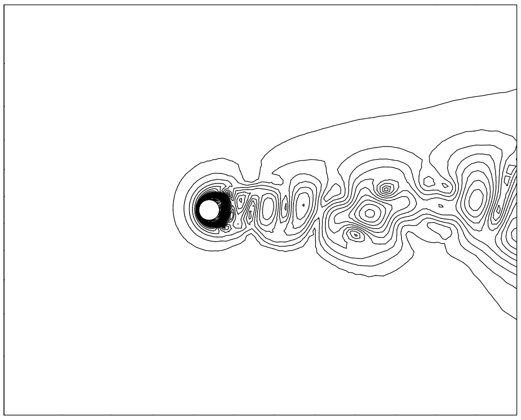

FIGURE 20. Mode velocity contours (example 2)

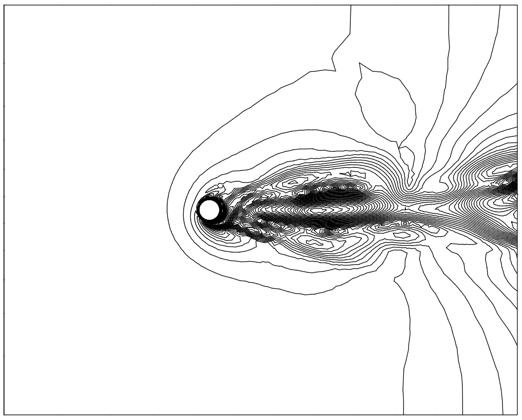

FIGURE 21. Mode velocity contours (example 3)

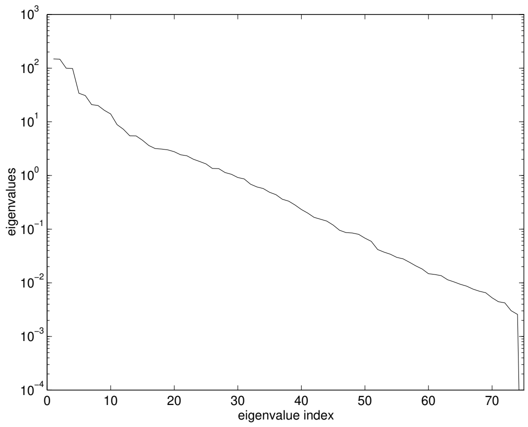

FIGURE 22. Eigenvalue spectrum (chirp excitation, unforced initial condition)

elements. In essence, we need to vary the phase of the vortex shedding at the cylinder, so that the unsteady dynamics of the system are reflected in the snapshots.

In order to carry out this system identification procedure the cylinder rotation

$$\gamma = \gamma_o sin[\frac{2\pi t}{T_1} + A\pi sin(\frac{2\pi t}{T_2})] \tag{5.1}$$

essentially a varying frequency sinusoid, or 'chirp' is imposed. The example shown in figure 17 ($\gamma_o = 2, T_1 = 6, A = 1, T_2 = 48$) yields excitation from around half to twice the shedding frequency. This chirp is used with two different initial conditions. The first is the locked-on flow. In this case, the angular velocity of the cylinder is required to remain continuous, so the chirp is constrained to start when $\gamma = 0$. The second initial condition is the steady vortex-shedding flow with a stationary cylinder. In this case the starting time is arbitrary. During the course of the chirp 75 snapshots are taken at time intervals 0.64 (starting at t=0.64), and these are used to form either the standard correlation matrix (for the penalty method) or the correlation matrix with homogeneous boundary condition snapshots (for the control function method).

The eigenvalue spectrum of the standard correlation matrix for the locked-on initial condition snapshots is shown in figure 18. Clearly, the varying-frequency cylinder rotation results in a flow with many more degrees of freedom (based on energy distribution) than the steady-state shedding. Figures 19 to 21 show some examples of the associated basis function velocity contour plots. From these it may be seen that our goal of generating basis functions capable of providing a more "physical" description of the flow has, at least to some extent, been attained. The presence of nearly frozen patterns convecting downstream may be accounted for by modes like those of figure 19, while other modes are dominated by local behavior around the cylinder (e.g.figure 20). Any changes in the mean flow due to the varying excitation also appear in the basis functions (e.g. figure 21).

The chirp excitation approach is equally successful in exciting a large number of degrees of freedom in the flow starting from the stationary cylinder condition. The eigenvalue spectrum for the (standard) correlation matrix is shown in figure 22, and is seen to have a very similar shape to that of figure 18. Equally, although the corresponding basis functions differ in detail from those shown in figures 19-21 , they exhibit a broad similarity in their general form, and we conclude that, in this case too, we have generated a mode set capable of describing the unsteady flows that will result from control action.

Turning to the basis functions derived for the control function method, we note that the control function $\mathbf{u}_c$ introduced in (4.1) is very nearly the r^{-1} Stokes vortex, and is quite localized around the cylinder. Given this, one would expect to see little difference in the general form of the eigenvalue spectra, and of the basis functions in regions away from the cylinder. On performing the POD on the modified snapshots this is indeed found to be the case.

5.1. *Effect of Basis Function Generalization on Model Performance*

5.1.1. *Performance measures*

The greater spread of energy in the chirp-excited snapshots implies a need for a greater number of basis functions in our low order model. Here we take 18, as a compromise between model complexity and flow description accuracy (around 98% of the unsteady energy in the snapshots is captured by the first 18 basis functions). Assessment of our results by comparing predicted and observed modal amplitudes is thus no longer practical and we seek to define more global performance measures.

We consider three velocity fields; the "exact" field $\mathbf{u}(\mathbf{x}, t)$ produced by the numerical simulation, the projected field $\mathbf{u}_p(\mathbf{x},t)$ and the predicted field $\hat{\mathbf{u}}(\mathbf{x},t)$. The second of these is the result of projecting onto the basis functions:

$$\mathbf{u}_p(\mathbf{x},t) = \mathbf{u}_m(\mathbf{x}) + \sum_{i=1}^{N} y_i(t)\boldsymbol{\Psi}_i(\mathbf{x}) \tag{5.2}$$

with

$$y_i = (\mathbf{u} - \mathbf{u}_m, \boldsymbol{\Psi}_i) \tag{5.3}$$

This differs from $\mathbf{u}(\mathbf{x},t)$ because of the inability of the $\boldsymbol{\Psi}_i$ to reproduce $\mathbf{u}-\mathbf{u}_m$ perfectly. The predicted field,

$$\hat{\mathbf{u}}(\mathbf{x},t) = \mathbf{u}_m(\mathbf{x}) + \sum_{i=1}^{N} \hat{y}_i(t)\boldsymbol{\Psi}_i(\mathbf{x}) \tag{5.4}$$

differs further, in that the $\hat{y}_i$ are the estimates obtained from the low order model, rather than the exact values obtained by projection. In the control function formulation, the corresponding expressions are

$$\mathbf{u}_p(\mathbf{x},t) = \mathbf{u}_m(\mathbf{x}) + \gamma(t)\mathbf{u}_c(\mathbf{x}) + \sum_{i=1}^{N} y_i(t)\boldsymbol{\Psi}_i(\mathbf{x}) \tag{5.5}$$

with

$$y_i = (\mathbf{u} - \mathbf{u}_m - \gamma\mathbf{u}_c,\ \boldsymbol{\Psi}_i) \tag{5.6}$$

and

$$\hat{\mathbf{u}}(\mathbf{x},t) = \mathbf{u}_m(\mathbf{x}) + \gamma(t)\mathbf{u}_c(\mathbf{x}) + \sum_{i=1}^{N} \hat{y}_i(t)\boldsymbol{\Psi}_i(\mathbf{x}) \tag{5.7}$$

Based on these velocity fields, we define two error measures. The projection error, E_p, is given by

$$E_p = \frac{(\mathbf{u} - \mathbf{u}_p,\ \mathbf{u} - \mathbf{u}_p)}{(\mathbf{u} - \mathbf{u}_m,\ \mathbf{u} - \mathbf{u}_m)} \tag{5.8}$$

and the prediction error, $\hat{E}$, by

$$\hat{E} = \frac{(\mathbf{u} - \hat{\mathbf{u}},\ \mathbf{u} - \hat{\mathbf{u}})}{(\mathbf{u} - \mathbf{u}_m,\ \mathbf{u} - \mathbf{u}_m)} \tag{5.9}$$

The normalization is chosen on the (estimated) velocity fluctuation $\mathbf{u} - \mathbf{u}_m$ to avoid the numerical "swamping" effect of including the mean flow. Since $\mathbf{u}_m$ is, to all intents and purposes, the same for the control function and penalty methods (it differs only in so far as the mean value of γ among the snapshots differs from zero) these measures will provide a valid basis for comparison.

Finally, we note that the orthogonality of the basis functions may be used to simplify equation (5.8);

$$E_p = \frac{(\mathbf{u}-\mathbf{u}_m,\ \mathbf{u}-\mathbf{u}_m) - \sum_{i=1}^{N} y_i^2}{(\mathbf{u}-\mathbf{u}_m,\ \mathbf{u}-\mathbf{u}_m)} \tag{5.10}$$

for the penalty method, and

$$E_p = \frac{(\mathbf{u}-\mathbf{u}_m-\gamma\mathbf{u}_c,\ \mathbf{u}-\mathbf{u}_m-\gamma\mathbf{u}_c) - \sum_{i=1}^{N} y_i^2}{(\mathbf{u}-\mathbf{u}_m,\ \mathbf{u}-\mathbf{u}_m)} \tag{5.11}$$

for the control function method. This quantity, resulting as it does from the exact projection of the flow onto the basis functions, will always be less than or equal to $\hat{E}$.

5.1.2. *Test Cases*

The first test case we consider is halting the cylinder after the steady state locked-on condition has been achieved; this is the example which demonstrated the inability of our original basis functions to follow the flow behavior (Sec. 4.5). We simulate this case using the generalized basis functions derived from the locked-on initial condition. Figures 23 and 24 show the time evolution of our error measures from the moment at which the cylinder is halted. (The control function method results are plotted in figure 23, and those for the penalty method in figure 24.) In each case the initial projection error is very low, confirming that the initial condition may be closely approximated by the basis functions used here. However, as the flow evolves the performance of the basis functions becomes less satisfactory, and the projection error is close to 20% by t=12. The prediction error, inevitably greater than the projection error, diverges from it at a rate which appears to increase with the projection error (as one might intuitively expect). Eventually the flow reaches a steady-state and the projection error saturates, but the prediction error continues to increase.

When the same test case is simulated using the generalized basis functions derived from the unforced initial condition, we observe similar general features (figures 25 and 26). Now, however, the differences in the snapshots used for the POD are reflected in the larger projection error at the initial condition. This projection error initially rises, and then eventually settles to a level of around 10% as the flow returns to the steady, unforced vortex shedding condition. Meanwhile, the prediction error shows a steady divergence from the projection error, and is generally larger than the corresponding quantity in figures 23 and 24.

In potential control applications, we are likely to be considering cylinder rotation started from rest, rather than the locked-on condition. We therefore consider a second test case, with the cylinder initially at rest, and then set into the same motion as was used to drive the steady locked on flow

$$\gamma = 2sin(\frac{2\pi t}{6}) \tag{5.12}$$

The starting flow here is the one used for the generation of the unforced initial condition basis function set. Figures 27 to 30 show the corresponding error measures for the low order models derived from the two basis function sets. Here the roles of the basis functions in the first test case are reversed, in that the initial flow is better described by the unforced initial condition set. (Interestingly, though, this set also captures the locked-on flow very effectively.) The prediction errors show similar trends to the sudden-halt

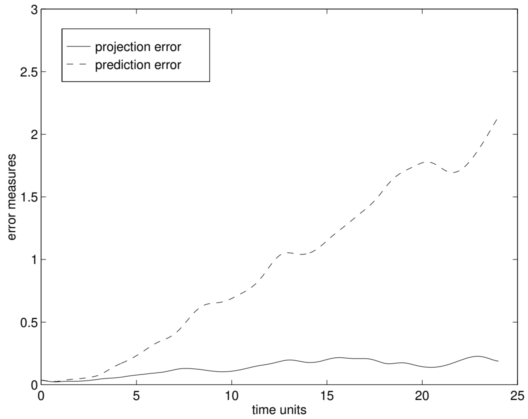

FIGURE 23. Sudden halt flow errors (control function method, locked-on initial condition basis functions)

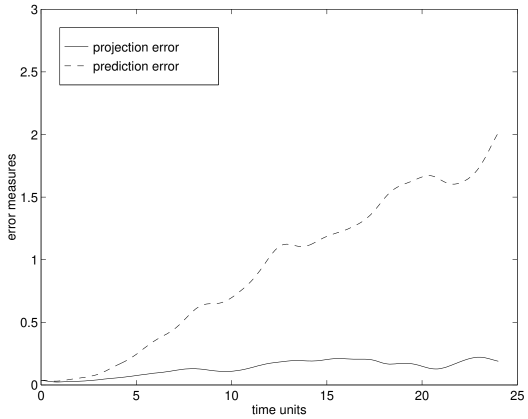

FIGURE 24. Sudden halt flow errors (penalty method, locked-on initial condition basis functions)

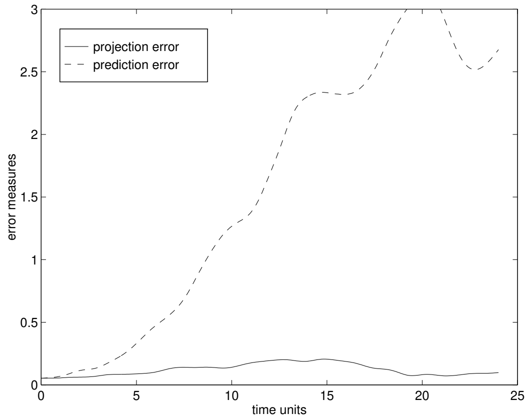

FIGURE 25. Sudden halt flow errors (control function method, unforced initial condition basis functions)

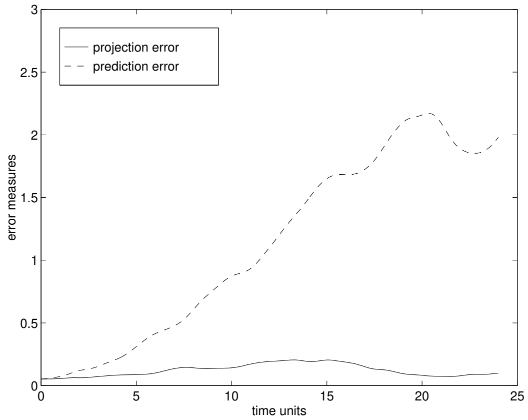

FIGURE 26. Sudden halt flow errors (penalty method, unforced initial condition basis functions)

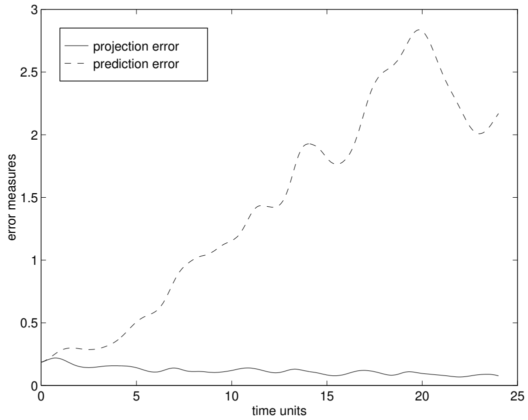

FIGURE 27. Start-up flow errors (control function method, locked-on initial condition basis functions)

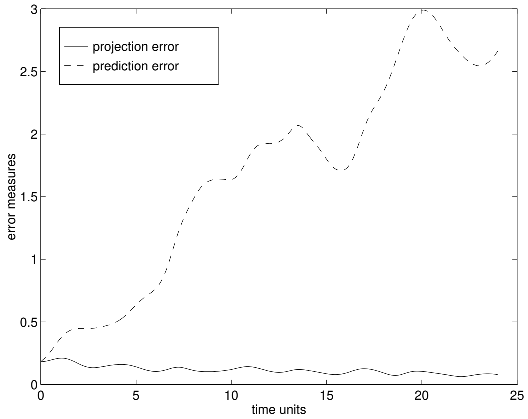

FIGURE 28. Start-up flow errors (penalty method, locked-on initial condition basis functions)

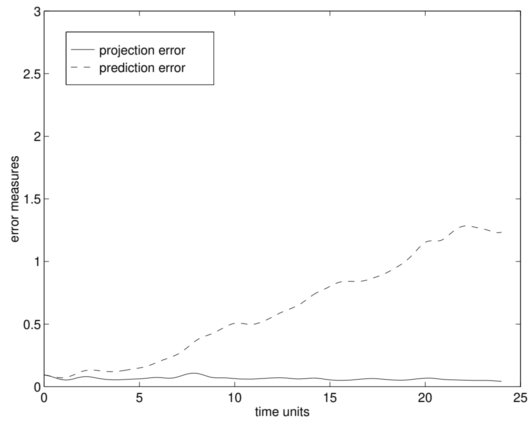

FIGURE 29. Start-up flow errors (control function method, unforced initial condition basis functions)

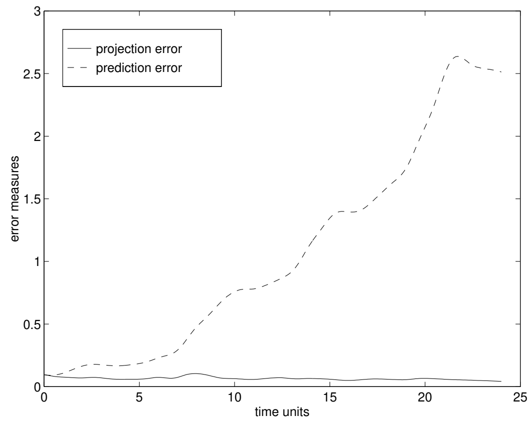

FIGURE 30. Start-up flow errors (penalty method, unforced initial condition basis functions)

results with the notable exception of figure 29 where the error remains somewhat lower. Since the unforced initial condition basis functions used in this example are derived from a situation similar to the start-up flow we would intuitively expect better results here. However, the penalty method (figure 30) does not show the same success. The reason for this is not clear, but we speculate that it may be linked to the stronger coupling between cylinder rotation and basis function amplitudes found in this method. Note, however, that a considerable contribution to the prediction error arises from phase errors, and general trends in mode amplitude evolution are often still successfully captured even when the error has reached high levels.

While these results clearly show more satisfactory behavior than that described in Sec. 4.5, they also demonstrate that the transient flows of these test cases cannot be perfectly captured by either set of basis functions. In the following section we discuss the implications of this conclusion as far as attempting to control the flow is concerned.

5.2. *Discussion*

The results of figures 23 to 30 demonstrate firstly, that low order models derived from our generalized basis function sets can be said to capture the dynamics of the flow (inspection of predictions and projections for individual mode amplitudes confirms this assertion), but secondly, that their ability to do so decreases with increasing time, and more rapidly for basis functions which are less able to describe the flow field. This implies that any form of model-based control must be reset periodically, to re-initialize the predictions for the mode amplitudes. Furthermore, the allowable time between resets, and the performance of the control during this time will depend on the quality of the basis function set in use and thus, by implication, on the system identification procedure used in its generation. As far as the comparison between the control function and penalty methods is concerned, no clear winner emerges from these test cases. The effectiveness of the prediction appears to depend more on the basis function set than the low order model formulation.

6. Conclusions

In this paper we have considered the application of the Proper Orthogonal Decomposition (POD) and Galerkin projection methods to generate low order models which include and successfully predict the effect of control action on a flow. This has necessitated two extensions to the customary implementation of this approach; the imposition of the non-homogeneous boundary conditions representing the control surface motion, and the generation of a broader, "generalized" set of basis functions capable of describing the associated transient flows.

Two methods for implementing the first extension have been proposed. In the control function approach, a velocity field satisfying the inhomogeneous boundary conditions is subtracted from the flow "snapshots" used in the POD (thus yielding basis functions satisfying a homogeneous boundary condition) and then included in the velocity field expansion, equation (4.2). The boundary conditions are thereby satisfied exactly and explicitly. By contrast, the penalty method converts the boundary conditions to a normal derivative, which is imposed in a weak implicit sense. Since each approach has its own advantages, both have been retained.

The second extension, generalized basis functions, is achieved by exciting the flow by "representative" control action, a roughly analogous process to transfer function determination in linear systems. The non-linear, and potentially high degree-of-freedom nature of our flow means that this process is dependent not only on the control action chosen, but also on initial conditions, and no attempt has been made to optimize this process. However, the use of a varying-frequency sinusoid (a chirp) has been found to produce the desired broadening of the basis function set for two different initial conditions; locked-on and unforced steady vortex shedding. The low-order models derived from these extensions have been applied to two transient flow test cases; halting the cylinder rotation when the flow is in a locked-on state, and starting a sinusoidal cylinder rotation from the unforced state. In each case, the models show the ability to follow the transient for a certain length of time, before prediction errors grow to a significant level. As one might expect, the rate of growth of the prediction errors appears to be closely linked to the projection error, which represents the extent to which the POD basis functions are unable to capture the flow.

As noted above, no attempt to optimize the generalized basis functions has been made, and we could certainly improve the behavior of our low order models for these test cases. However, this would be no guarantee of improved performance in controlling the flow, which is our aim. The predictive ability demonstrated here is sufficient to expect that we can successfully implement a model-based control strategy, given sufficient information to update the model periodically, and this task is described in the companion paper, Part II.

REFERENCES

Berger, E. 1967 Suppression of vortex shedding and turbulence behind oscillating cylinders. *Phys. Fluids Suppl.* **10**, S191–S193.

Berkooz, G., Holmes, P. & Lumley, J. L. 1993 The proper orthogonal decomposition in the analysis of turbulent flows. *Ann. Rev. Fluid Mech.* **25**, 539–575.

Bloxsidge, G. J., Dowling, A. P. & Langhorne, P. J. 1988 Reheat buzz: an acoustically coupled combustion instability. Part 2. Theory. *J. Fluid Mech.* **193**, 445–473.

Chicatelli, A. & Richard, J. C. 1993 Reduced order linear modeling of supersonic compression and propulsion systems dynamics. NASA TM-106090.

Chorin, A. J. 1969 Numerical solution of the Navier-Stokes equations. *Math. Comp.* **23**.

Christie, I., Griffiths, D. F., Mitchell, A. R. & Zienkiewicz, O. C. 1976 Finite element methods for second order equations with significant first derivatives. *Int. j. numer. methods eng.* **10**, 1389–1396.

Coller, B. D., Holmes, P. & Lumley, J. L. 1994 Control of bursting in boundary-layer models. *Appl. Mech. Rev.* **47(6)**, 139–143.

Day, I. J. 1993 Active suppression of rotating stall and surge in axial compressors. *ASME J. Turbomach.* **115**, 40–47.

Deane, A. E., Kevrekidis, I. G., Karniadakis, G. E. & Orszag, S. A. 1991 Low-dimensional models for complex geometry flows: Application to grooved channels and circular cylinders. *Phys. Fluids* **A 3(10)**, 2337–2354.

Donea, J. 1984 A Taylor-Galerkin method for convective transport problems. *Int. j. numer. methods eng.* **20**, 101–119.

Donea, J., Giuliani, S., Laval, H. & Quartapelle, L. 1982 Finite element solution of the unsteady Navier-Stokes equations by a fractional step method. *Comp. Meth. Appl. Mech. Engng.*, 53–73.

Duncan, W. J., Thom, A. S. & Young, A. D. 1970 *Mechanics of Fluids*. American Elsevier Publishing Co.

Ffowcs Williams, J. E. & Huang, X. 1989 Active stabilization of compressor surge. *J. Fluid Mech.* **204**, 245–262.

Ffowcs Williams, J. E. & Graham, W. R. 1990 An engine demonstration of active surge control. *ASME Paper* **90-GT-224**.

Glezer, A., Kadioglu, Z. & Pearlstein, A. J. 1989 Development of an extended proper orthogonal decomposition and its application to a time periodically foced plane mixing layer. *Phys. Fluids* **A 1(8)**, 1363–1373.

Golub, G. H. & Van Loan, C. 1981 *Matrix Computations*. Academic Press.

Gysling, D. L., Dugundji, J., Greitzer, E. M. & Epstein, A.H. 1991 Dynamic control of centrifugal compressor surge using tailored structures. *ASME J. Turbomach.* **113**, 710–722.

Hall, K. C. 1994 Eigenanalysis of unsteady flows about airfoils, cascades and wings. Presented at the *AIAA Structures, Structural Dynamics and Materials Conference*, Hilton Head, South Carolina.

Hall, K. C., Florea, R. & Lanzkron, P. J. 1994 A reduced order model of unsteady flows in turbomachinery. Presented at the *39th ASME International Gas Turbine Congress and Exhibition*, The Hague.

Hughes, T. J. R. & Brooks, A. N. 1979 A multidimensional upwind scheme with no cross-wind diffusion, in *Finite Element Methods for Convection Dominated Flows* (ed. T. J. R. Hughes). AMD-Vol. 34, ASME, New York.

Langhorne, P. J. 1988 Reheat buzz: an acoustically coupled combustion instability. Part 1. Experiment. *J. Fluid Mech.* **193**, 417–443.

Langhorne P. J., Dowling, A. P. & Hooper, N. 1990 Practical active control system for combustion oscillations. *J. Propuls.* **6**, 324–333.

Monkewitz, P. A., Berger, E. & Schumm, M. 1991 The nonlinear stability of spatially inhomogeneous shear flows, including the effect of feedback. *Eur. J. Mech., B/Fluids* **10(2)-Suppl.**, 295–300.

Moore, F. K. & Greitzer, E. M. 1986 A theory of post-stall transients in axial compressors: Part I - Development of equations. *ASME J. Eng. Gas Turbines Power* **108**, 68–76.

Paduano, J. D., Epstein, A. H., Valavani, L., Longley, J. P., Greitzer, E. M. & Guenette, G. R. 1993 Active control of rotating stall in a low-speed axial compressor.

ASME J. Turbomach. **115**, 48–56.

PINSLEY, J. E., GUENETTE, G. R., EPSTEIN, A. H. & GREITZER, E. M. 1991 Active stabilization of centrifugal compressor surge. *ASME J. Turbomach.* **113**, 723–732.

RAJAEE, M., KARLSSON, S. K. F. & SIROVICH, L. 1994 Low-dimensional description of free-shear-flow coherent structures and their dynamical behaviour. *J. Fluid Mech.* **258**, 1–29.

SIMO, J. C. & ARMERO, F. 1994 Unconditional stability and long-term behaviour of transient algorithms for the incompressible Navier-Stokes and Euler equations. *Comput. Methods Appl. Mech. Engrg.* **111**, 111–154.

SIROVICH, L. 1987 Turbulence and the dynamics of coherent structures, Part I: Coherent structures, Part II: Symmetries and transformations, Part III: Dynamics and scaling. *Q. Appl. Math.* **45(3)**, 561–571, 573–582, 583–590.

TANG K. Y. 1996 Numerical simulation and control of separated incompressible flows. Master thesis, M.I.T.

ZIENKIEWICZ, O. C. & MORGAN, K. 1982 *Finite Elements and Approximation.* Wiley.

ZIENKIEWICZ, O. C., SZMELTER, J. & PERAIRE, J. 1990 Compressible and incompressible flow; an algorithm for all seasons. *Comp. Meth. Appl. Mech. and Engng.* **78**, 105–121.